crystals

MDPI

Article

Mineral Characterization in Human Body: A Dual Energy Approach

Niki Martini, Vaia Koukou, Christos Michail and George Fountos *

Radiation Physics, Materials Technology and Biomedical Imaging Laboratory, Department of Biomedical Engineering, University of West Attica, Ag. Spyridonos, 12210 Athens, Greece; mmartini@uniwa.gr (N.M.); koukou@uniwa.gr (V.K.); cmichail@uniwa.gr (C.M.)

* Correspondence: gfoun@uniwa.gr; Tel.: +30-210-5385387

Abstract: Kidney and uteric stones are a common cause of pain and disturbance in numerous people worldwide, as they tend to reappear. There are several studies investigating the association of urolithiasis and nephrolithiasis with atherosclerosis, as patients suffering from the former diseases were found to have been diagnosed with atherosclerotic plaques. Hydroxyapatite and calcium oxalate are the most common mineral crystals found in both kidney/uteric stones and atherosclerotic plaques' calcifications. Even though for stones smaller than 5 mm surgery is not recommended, the knowledge of the stone composition is an important tool for the physician in order to provide better treatment for the patient. The mineral crystal characterization of atherosclerotic plaques' calcifications smaller than 3 mm (spotty calcifications) will assist the physician to limit the possibility of myocardial infraction and stroke, as the presence of hydroxyapatite indicates possible plaque rapture. To this aim, a dual energy (DE) X-ray method was developed in this work. The calcium/phosphorus mass ratio (m_{Ca}/m_P) was determined through analytical simulations and the results were verified experimentally. Both monoenergetic and polyenergetic simulation studies were implemented for hydroxyapatite, calcium carbonate and calcium oxalate with thicknesses ranging from 0.50 to 3.00 mm, at 100 μm increments, to obtain the optimized irradiation conditions. The experimental verification of the proposed method was performed using an X-ray tube combined with a high resolution complementary metal-oxide-semiconductor (CMOS) active pixel sensor (APS) detector. The Mann–Whitney U test indicated that statistically significant differences were found between the different types of minerals examined for thicknesses of 0.70 mm or higher.

Keywords: dual energy; X-ray; kidney stones; atherosclerotic plaques; minerals; calcium oxalate; hydroxyapatite; calcium carbonate; calcium/phosphorus mass ratio

check for updates

Citation: Martini, N.; Koukou, V.; Michail, C.; Fountos, G. Mineral Characterization in Human Body: A Dual Energy Approach. *Crystals* **2021**, *11*, 345. https://doi.org/10.3390/cryst11040345

Academic Editor: Andrew V. Martin

Received: 26 February 2021
Accepted: 25 March 2021
Published: 28 March 2021

Publisher's Note: MDPI stays neutral with regard to jurisdictional claims in published maps and institutional affiliations.

Copyright: © 2021 by the authors. Licensee MDPI, Basel, Switzerland. This article is an open access article distributed under the terms and conditions of the Creative Commons Attribution (CC BY) license (https://creativecommons.org/licenses/by/4.0/).

1. Introduction

Urolithiasis and nephrolithiasis are frequent causes of intense pain affecting higher percentages of the population and increasing the expenses for health systems [1–3]. Based on previous works, the majority of ureteric and kidney stones will pass spontaneously, especially when they are smaller than 5 mm [4–8]. In this case, no external assistance is needed. On the other hand, when a stone cannot pass spontaneously, elective surgery will be applied [3]. It is not only the presence of stones but also the repetition of their presence in the patients that urge the physicians in deeper learning of stones' pathophysiology through investigation over their composition [9,10]. The known stone composition will lead to patients' better treatment since the appropriate strategy will be followed for each patient and unneeded operation may be prevented [3,9–14]. The earlier the stone is found, the lower the probability of an operation and reappearance [10,15–17]. Calcium oxalate minerals are most commonly found in kidney/ureteric stones, followed by hydroxyapatite [9,10,18–28]. Calcium carbonate can also be found in stones; however, its presence is rare enough [23,29,30]. Computed Tomography (CT) is the gold standard method for kidney stones diagnosis; however, it has difficulty in discriminating between different stone compositions [3,4,8–10,14,15,17,19].

Dual-energy Computed Tomography (DECT) is a promising technology with the potential to improve the differentiation of stone phenotypes by composition. Various studies have been implemented to this aim. Primak et al. determined the accuracy and sensitivity for the discrimination of uric acid stones from other non-uric acid renal stones in a commercially available dual-energy CT system. They used three anthropomorphic phantom models of different sizes (medium, large, extra-large) and concluded that dual-energy CT can accurately discriminate uric acid stones from other stone types [19]. A review study of Eliahou et al. described the role of DECT for in vitro and in vivo analysis of calcium, uric acid and cystine stones. DECT in vitro can add valuable information to the characterization of urinary calculi [9]. However, few in vivo studies have been performed showing that uric acid, calcium and cysteine stones could be differentiated but struvite stones and calcium oxalate subtypes could not [31,32]. Zilberman et al. assessed DECT combined with post-image processing for the differentiation of urinary calculi in vivo and suggested that it can accurately discriminate between different types in vivo including calcium containing subgroups [13]. Li et al. compared DECT and CT at 120 kV by comparing the attenuation values of seven pure stone phenotypes. The results showed that there was still some overlap between the ranges of calcium oxalate monohydrate and dihydrate, struvite and cystine, and calcium phosphate and brushite. However, the overall value between all seven stone phenotypes was statistically different when analyzed at 50 keV [14]. Wisenbaugh et al. compared the accuracy between conventional CT and DECT in predicting stone composition in a blinded prospective fashion. Twenty-seven stones were analyzed with different composition types. DECT appeared to be superior to single CT in differentiating non-uric acid from uric acid stones [15].

Most of the severe myocardial infarction [33,34] and stroke incidents [35] happen due to the rupture of atherosclerotic plaques. The atherosclerotic plaques' vulnerability is associated with their heterogeneity in formation, including a necrotic core, a fibrous cap, inflammatory cells and calcifications [36,37]. The calcification of coronary arteries is provoked by inflammation and serves as the elementary stage of atherosclerotic plaque [38–42]. Calcifications are not only considered to be clinical indicators of atherosclerotic plaques [43], but are also associated with their mechanical behavior and process [44,45]. Previous studies have identified that the two main calcium mineral crystals found in atherosclerotic plaques are hydroxyapatite [42,43,45–54] and calcium oxalate [42,50,55], with the former noted as the dominant calcification mineral crystal [56]. According to Bischetti et al. [57], the presence of calcium oxalate in atherosclerotic plaques is correlated with stable plaques, while hydroxyapatite was found in either stable or unstable plaques. Apart from hydroxyapatite and calcium oxalate, Creager et al. [42] studied calcium carbonate as an atherosclerotic calcification mineral crystal. Motoyama et al. [58] in their study defined calcifications, with sizes smaller than 3 mm, found on CT multiplanar reconstruction images as "spotty" calcifications [43,59,60]. Spotty calcifications are also found to be connected with extensive and expanded atherosclerosis and quick disease progression [61,62]. CT is the non-invasive gold standard method to detect calcifications, and as such, it is the most used imaging modality for the screening of patients who suffer from or are suspected to suffer from atherosclerosis [37,45,58,63–66].

DECT is also used for the imaging of coronary arteries since it has the ability to better characterize atherosclerotic plaques compared to CT through plaque components' discrimination. Barreto et al. worked on the classification of atherosclerotic plaques' components. They used DECT in order to image human coronary arteries ex vivo and compared their results with those of histology. The results showed that discrimination between dense calcified and non-calcified plaques could be accomplished [67]. Boll et al. investigated the capability of DECT, accompanied by new postprocessing techniques, to quantify small, calcified plaques compared to Optical Coherence Tomography (OCT). They concluded that pathodynamic phenomena related to vulnerable plaques could possibly be prognosed since the calcified plaques were more accurately quantified with their technique [68]. Henzler et al., by using human specimens, explored the feasibility of atherosclerotic plaques' characterization on a density basis. The results of this study were compared to histopathology findings. Their results indicated that they could discriminate atheroma, fibroatheroma and calcific plaques [69]. Nakajima et al. proposed the use of the effective atomic number as an indicator for differentiation between soft and fibrous non-calcified coronary plaques. Compared to the Hounsfield unit-based differentiation obtained when CT is used, effective atomic number-based differentiation with the use of DECT resulted in more accurate classification of the plaques [70]. The effective atomic number was also used by Nishizawa et al. in an in vivo study in an attempt to analyze the calcific lesions' composition. They concluded that although hydroxyapatite is mostly found in plaques' calcifications, calcium oxalate was found in the majority of atherosclerotic plaques of dialysis patients [63]. Ding et al. conducted a simulation study to investigate if three and four material decomposition with the use of DECT could lead to composition analysis of atherosclerotic plaques. Three and four low atomic number materials were used in three and four material decomposition, respectively. The results showed that the proposed technique has the potential to quantify the atherosclerotic plaques' composition [71].

Even though kidney stones are not fatal, they may provoke cardiovascular diseases that are among the diseases with the highest mortality rates [72,73]. Several studies investigated the association between urolithiasis/nephrolithiasis and cardiovascular diseases including atherosclerotic plaques [72–78]. Aydin et al. investigated data from two hundred patients with kidney stones composed of calcium oxalate and two hundred controls to estimate the ten-year risk of cardiovascular disease and mortality. The results indicated higher risk for both cardiovascular disease and mortality for the patients that had a history of kidney stones compared to controls [75]. Davarajan published a review paper presenting the studies correlating kidney stones to cardiovascular diseases, and especially atherosclerosis. This review paper clarifies how kidney stones lead to atherosclerosis and atherosclerosis to kidney stones. Based on all the preclinical and clinical studies included in this research, the association between these two diseases is a two-way process [73]. Huang et al. worked on the assumption that the presence of atherosclerotic plaques is related to the existence of kidney stones in a patient, and especially stones composed of calcium. They studied the relation of serum total cholesterol, high-density lipoprotein cholesterol, and low-density lipoprotein cholesterol on twenty-four-hour urine chemical components and calcium composed stones. The evaluation of the association between calcium composed stones, serum cholesterol levels and the extent of atherosclerotic plaques was accomplished by comparing the results with the controls. The results indicated that there was significant correlation between calcium composed kidney stones and atherosclerotic plaques [76]. Luo et al. in their review paper collected and presented the results of numerous studies investigating the association between urolithiasis and atherosclerotic plaques. More than 70,000 samples were examined in all these studies. The assessment of all the studies' results revealed that the possibility of atherosclerotic plaque formation when ureteric stones were found in the samples was higher [79]. Although the association between ureteric/kidney stones and atherosclerotic plaques requires more investigation, the screening for cardiovascular diseases in patients with ureteric/kidney stones shall be taken into consideration [77,78].

Our research team has worked on the discrimination between the different mineral crystals found in breast cancer [79,80]. Calcium oxalate is the mineral crystal found in Type I breast calcifications and is associated with benignancy [81,82]. Type II malignant breast calcifications are composed of hydroxyapatite, while the presence of calcium carbonate in Type II indicates benignancy [83–85]. The differentiation was accomplished through the estimation of the effective calcium/phosphorus mass ratio (m_{Ca}/m_P) with the dual energy (DE) X-ray method that we developed. Since phosphorus is present only in hydroxyapatite, an effective m_{Ca}/m_P was estimated for calcium carbonate and calcium oxalate [79]. The method was experimentally evaluated with the use of photon counting energy dispersive and energy integrating detectors [80,86,87]. There was a statistically significant difference between the minerals examined for calcifications 300 µm thick or higher.

In the present study, a dual energy X-ray method was developed in order to discriminate between calcium composed kidney/ureteric stones. The proposed method was also used to differentiate the calcium composed atherosclerotic plaques. In both cases, m_{Ca}/m_P was estimated. Simulation monoenergetic and polyenergetic studies were conducted based on a previously validated modified analytical model to obtain the optimized irradiation conditions. The method was experimentally verified with the use of an X-ray tube combined with a high resolution complementary metal-oxide-semiconductor (CMOS) active pixel sensor (APS) detector. The results of the study indicate that the differentiation of hydroxyapatite, calcium carbonate and calcium oxalate is feasible when m_{Ca}/m_P is used as a differentiation parameter.

2. Materials and Methods

2.1. Simulation Study

2.1.1. Monoenergetic Beams

The analytical model of the study calculated the attenuated intensities for the low-/high-energy beams as follows. Assume that along the monoenergetic X-ray path a torso of thickness T consists of: (i) surrounding tissue t_s and (ii) kidney/uteric stone or calcification in atherosclerotic plaque t_c (Figure 1). The surrounding tissue was simulated using attenuation coefficients of water. Since the phantoms of kidney/uteric stones and calcifications in atherosclerotic plaque were composed of a mixture of mineral and epoxy resin, the same quantity of epoxy resin was also used in the surrounding tissue. Thus, when only surrounding tissue was in the path of the X-ray beam, the low-/high-energy intensities, $I_{s,El}$ and $I_{s,Eh}$, were calculated as:

$$I_{s,Ei} = I_{o,Ei}e^{-\mu_{s,Ei}T} \quad i = l,\ h. \tag{1}$$

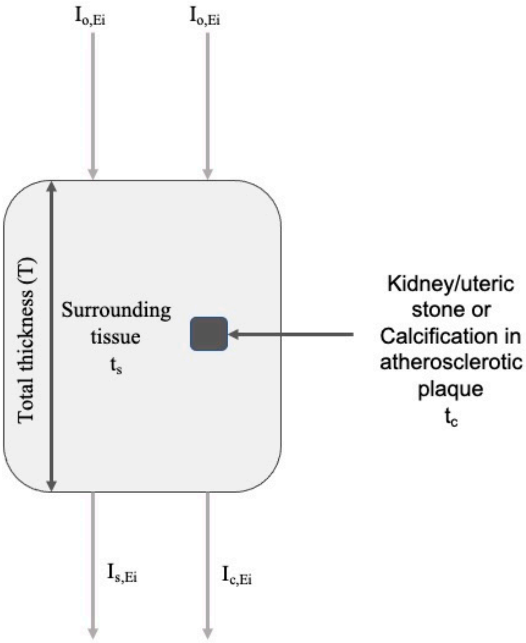

Figure 1. Schematic representation of the attenuated intensities, $I_{s,Ei}$ and $I_{c,Ei}$, calculation.

When both surrounding tissue and kidney/uteric stone or calcification in atherosclerotic plaque were in the path of the X-ray beam, the low-/high-energy intensities, $I_{c,El}$ and $I_{c,Eh}$, were calculated as:

$$I_{c,Ei} = I_{o,Ei}e^{-\mu_{s,Ei}t_w-\mu_{mineral,Ei}t_c} \quad i = l,\ h. \tag{2}$$

where $I_{o,El}$ and $I_{o,Eh}$ are the unattenuated intensities for the low and high energy, respectively. The energy-dependent linear attenuation coefficients (cm^{-1}) and thickness (cm) for the surrounding tissue and the mineral crystals were given by $\mu_{s,Ei}$, $\mu_{mineral,Ei}$ and t_s, t_c, respectively.

For both kidney/uteric stones and calcifications in atherosclerotic plaque, three different types of mineral crystals were investigated: (i) hydroxyapatite ($Ca_{10}(PO_4)_6(OH)_2$), HAp, with a density of 3.18 g cm^{-3} [88], (ii) calcium carbonate ($CaCO_3$) with a density of 2.93 g cm^{-3} [89], and (iii) calcium oxalate (CaC_2O_4) with a density of 2.20 g cm^{-3} [90]. The epoxy resin ($C_{19}H_{23}ClO_4$) used in the simulation study had a density of 1.06 g cm^{-3} (Resoltech, Rousset, France) [91]. The mineral crystals are referred to as HAp, $CaCO_3$ and CaC_2O_4.

The unattenuated intensities, $I_{o,El}$ and $I_{o,Eh}$, for the low and high energy, respectively, were calculated through the entrance surface dose (K_a) (Equation (3)) for all photon energies between 40 and 140 keV at 1 keV increments, according to Equation (4).

$$K_a(mGy) = 8.77 \cdot 10^{-3} \cdot 1.83 * 10^{-6} \cdot I_{o,Ei} \cdot E_i \cdot \left(\frac{\mu_{en}}{\rho}_{Ei} \right)_{air} \tag{3}$$

$$I_{o,Ei} = K_a(mGy) / \left(8.77 \cdot 10^{-3} \cdot 1.83 \cdot 10^{-6} \cdot E_i \cdot \left(\frac{\mu_{en}}{\rho}_{Ei} \right)_{air} \right) \tag{4}$$

where $I_{o,Ei}$ is the unattenuated intensity (photons/mm^2) at energy E_i. The X-ray mass energy absorption coefficient of air, $(\mu_{en}/\rho)_{air}$, was obtained from the literature [92]. K_a was set at 8 mGy and was evenly split between the low-/high-energy.

The attenuated intensities, $I_{s,Ei}$ and $I_{c,Ei}$, were calculated with the use of energy-dependent linear attenuation coefficients, which were obtained by multiplying the mass attenuation coefficients from published data (NIST) [92] and the corresponding densities. In order to differentiate the mineral crystals, the attenuated intensities after passing through the torso were used. For both simulation and experimental studies, for every HAp thickness the equivalent thickness of $CaCO_3$ and CaC_2O_4 was defined, leading to equivalent attenuation. The examined HAp kidney/uteric stone and calcification in atherosclerotic plaque thicknesses ranged from 0.5 mm to 3 mm, at 100 µm increments. The thicknesses of calcium carbonate and calcium oxalate, which resulted in an equal number of photons after the attenuation, were calculated and averaged in order to obtain the corresponding equivalent thicknesses. The standard deviation (SD) of equivalent thicknesses, for both $CaCO_3$ and CaC_2O_4, was lower than 24.42 µm. The HAp thicknesses and the equivalent thicknesses of calcium carbonate and calcium oxalate are presented in Table 1 for a torso thickness of 20.8 cm [93–96].

Table 1. HAp, $CaCO_3$ and CaC_2O_4 thicknesses examined for kidney/uteric stones and calcifications in atherosclerotic plaques.

HAp	$CaCO_3$	CaC_2O_4	HAp	$CaCO_3$	CaC_2O_4
0.50	0.61	0.99	1.80	2.23	3.75
0.60	0.74	1.21	1.90	2.35	3.96
0.70	0.86	1.43	2.00	2.47	4.17
0.80	0.99	1.65	2.10	2.60	4.38
0.90	1.12	1.86	2.20	2.72	4.59
1.00	1.24	2.08	2.30	2.85	4.80
1.10	1.36	2.29	2.40	2.97	5.00
1.20	1.48	2.50	2.50	3.10	5.21
1.30	1.61	2.71	2.60	3.22	5.42
1.40	1.73	2.92	2.70	3.34	5.63
1.50	1.86	3.13	2.80	3.46	5.84
1.60	1.98	3.34	2.90	3.59	6.05
1.70	2.11	3.55	3.00	3.71	6.25

The effective calcium/phosphorus mass ratio (m_{Ca}/m_P) was calculated for all mineral crystal types using Equation (5) [79,97].

$$\frac{m_{Ca}}{m_P} = \frac{\left(Y_{El} * \Delta_{\mu PO_4,Eh}\right) - \left(Y_{Eh} * \Delta_{\mu PO_4,El}\right)}{\left(Y_{Eh} * \Delta_{\mu Ca,El}\right) - \left(Y_{El} * \Delta_{\mu Ca,Eh}\right)} \cdot 3.0679 \tag{5}$$

where $Y_{Ei} = \Delta_{\mu_{Ca,Ei}} t_{Ca} + \Delta_{\mu_{PO4,Ei}} t_{PO4}$ (i = l, h) for the low- and high-energy, respectively. $\Delta_{\mu_{Ca,Ei}} = \mu_{Ca,Ei} - \mu_{s,Ei}$ and $\Delta_{\mu_{PO4,,Ei}} = \mu_{PO4,Ei} - \mu_{s,Ei}$ (i = l, h) for the low- and high-energy, respectively. μ_{Ca}, μ_{PO4} and μ_s are the energy-depended linear attenuation coefficients (1 cm^{-1}) for calcium, phosphate and soft tissue, respectively.

For all calcification types, the m_{Ca}/m_P was estimated using the equation above. The modyfied analytical model of the present study calculates the m_{Ca}/m_P of HAp where both calcium and phosphorus are found in its molecule. However, phosphorus is not present in $CaCO_3$ and CaC_2O_4 molecules. Since the aim of the present study is to characterize an unknown mineral type based on attenuation intensity measurements, in the m_{Ca}/m_P calculation the linear attenuation coefficients of PO_4 are used, regardless of the calcification type. The m_{Ca}/m_P is mentioned as "effective" as the amount of CO_3 and C_2O_4 corresponds to a smaller amount of PO_4 in order to preserve equal photon beam attenuation. This is attributed to the fact that CO_3 and C_2O_4 have lower linear attenuation coefficients compared to PO_4 [79]. Hence, the calculated effective m_{Ca}/m_P for these mineral crystals is expected to be lower.

In an incident beam with a number of I photons (considering Poisson distribution), the coefficient of variation (CV) can be calculated as $CV = \sqrt{I}/I$. The use of the error theory and the performance of derivations [79] resulted in Equation (6) for the simulation study with analytical methods. The coefficient of variation of the effective m_{Ca}/m_P ($CV_{m_{Ca}/m_P}(\%)$) was calculated according to Equation (6) for all mineral crystals [79]. The minimization of $CV_{m_{Ca}/m_P}(\%)$ was the criterion to select the optimum energy pair. The $CV_{m_{Ca}/m_P}(\%)$ of each mineral crystal is referred to as $CV_{m_{Ca}/m_P,HAp}(\%)$, $CV_{m_{Ca}/m_P,CaCO_3}(\%)$ and $CV_{m_{Ca}/m_P,CaC_2O_4}(\%)$ for hydroxyapatite, calcium carbonate and calcium oxalate, respectively.

$$\begin{aligned}
CV^2{}_{m_{Ca}/m_P} = {} & \left(\tfrac{1}{I_{s,El}} + \tfrac{1}{I_{c,El}}\right) \\
& \cdot \left(\frac{\left(\Delta_{\mu PO_4,Eh}\right)^2}{\left(\left(Y_{El}*\Delta_{\mu PO_4,Eh}\right)-\left(Y_{Eh}*\Delta_{\mu PO_4,El}\right)\right)^2} + \frac{\left(\Delta_{\mu Ca,Eh}\right)^2}{\left(\left(Y_{Eh}*\Delta_{\mu Ca,El}\right)-\left(Y_{El}*\Delta_{\mu Ca,Eh}\right)\right)^2} \right) \cdot 100^2 \\
& + \left(\tfrac{1}{I_{s,Eh}} + \tfrac{1}{I_{c,Eh}}\right) \cdot \left(\frac{\left(\Delta_{\mu PO_4,El}\right)^2}{\left(\left(Y_{El}*\Delta_{\mu PO_4,Eh}\right)-\left(Y_{Eh}*\Delta_{\mu PO_4,El}\right)\right)^2} + \frac{\left(\Delta_{\mu Ca,El}\right)^2}{\left(\left(Y_{Eh}*\Delta_{\mu Ca,El}\right)-\left(Y_{El}*\Delta_{\mu Ca,Eh}\right)\right)^2} \right) \cdot 100^2
\end{aligned} \tag{6}$$

2.1.2. Polyenergetic X-rays

Unfiltered spectra from TASMIP spectral models generated from a tungsten anode were used to obtain low-/high-energy spectra. The mean energies of the spectra should be similar to those indicated by the monoenergetic study [98]. The peak tube voltages were 50 kVp for the low energy and 90 kVp for the high energy. The examined filter materials for the low energy were selected based on their K-edges. In addition to these filters, aluminum was also examined. Although aluminum does not have a strong K-edge that could modify a spectrum into a quasi-monoenergetic spectrum, it is a common filter used in X-ray systems as it attenuates the low energies in spectra. In lanthanide filters, which are those with the most effective K-edges, there is no filter with a K-edge higher than 64 keV [79]. Hence, the selection of high energy filter materials was based on the filters' density. In Table 2, the filter materials with their K-edges and densities are presented for the low- and high-energy, respectively. All filter materials were examined for thicknesses ranging from 0.01 to 3 cm at 0.01 cm increments.

Table 2. Filter materials examined for the low and high energy.

Low Energy Filters		**High Energy Filters**	
Filter Material	**K-Edge (keV)**	**Filter Material**	**Density (g cm^{-3})**
Cerium (Ce)	40.44	Gallium (Ga)	5.90
Praseodymium (Pr)	41.99	Vanadium (V)	6.00
Neodymium (Nd)	43.57	Antimony (Sb)	6.69
Promethium (Pr)	45.18	Chromium (Cr)	7.18
Samarium (Sm)	46.83	Tin (Sn)	7.31
Europium (Eu)	48.52	Copper (Cu)	8.96
Aluminum (Al)	1.56	Bismuth (Bi)	9.75

The filters for the low-/high-energy were applied to unfiltered spectra obtained at 200 and 400 mAs, respectively. The Radcal 2026C (Radcal Corporation, Monrovia, CA, USA) ionization chamber [99] was placed at 66 cm from the tube output in order to measure the entrance surface doses for the low-/high-energy. The measured doses were 2.31 mGy and 30.50 mGy for the low-/high-energy, respectively.

A nonparametric statistical analysis was conducted with the use of the attenuated intensities ($I_{s,Ei}$ and $I_{c,Ei}$). Assuming Poisson distribution for the $I_{s,Ei}$ and $I_{c,Ei}$, 5000 random values were generated for each one, leading to 5000 effective m_{Ca}/m_P values. The calculations were accomplished for HAp, $CaCO_3$ and CaC_2O_4 in order to determine the distribution of m_{Ca}/m_P of each mineral crystal. Based on a previous work of our team, the normal Kernel distribution describes the random variable, effective m_{Ca}/m_P [79]. For all mineral crystal types and thicknesses, the Kernel probability functions were obtained and the false positive and false negative values were calculated.

2.2. Experimental Verification

2.2.1. Irradiation Process

The radiographic system Del Medical Eureka (DEL MEDICAL, Harrison, NY and Bloomingdale, IL, USA) with a tungsten (W) anode was used in the experimental evaluation of the method [100]. The low energy images were acquired at 50 kVp and 200 mAs with the inherent filtration of 3 mm aluminum, while the high energy images were acquired at 90 kVp, 400 mAs and added filtration of 3 mm 99.99% pure copper (Cu) foil. The detection system was a terbium-doped gadolinium oxysulfide (Gd_2O_2S:Tb) phosphor screen (Min-R 2190 with a mass thickness of 33.91 mg cm^{-2}) coupled to an optical readout device including a complementary metal-oxide-semiconductor (CMOS) Remote RadEye HR (Rad-icon Imaging Corp, Santa Clara, CA, USA) photodiode pixel array. The CMOS photodiode array has a format of 1200 × 1600 pixels. The active area is 27 × 36 mm^2, and the pixel pitch is 22.5 µm. The Gd_2O_2S:Tb screen was directly overlaid onto the active area of the CMOS [87]. The source-to-detector distance (SDD) was set at 66 cm. A schematic representation of the experimental configuration is illustrated in Figure 2.

The analytical model requires the total number of photons of the attenuated intensities for the determination of effective m_{Ca}/m_P. Thus, the pixel values of the low-and high-energy images should be converted to photons. To this aim, the detector response curve was measured and used in the conversion of pixel values to dose and finally to photons, since the $I_{s,Ei}$ and $I_{c,Ei}$ are known. Hence, Equation (3) is rewritten as [79,101]:

$$K_a(mGy) = 8.77 * 10^{-3} * \sum_{E_{min}}^{E_{max}} 1.83 * 10^{-6} * I_{Ei} * E_i * \left(\frac{\mu_{en}}{\rho}_{Ei}\right)_{air} \tag{7}$$

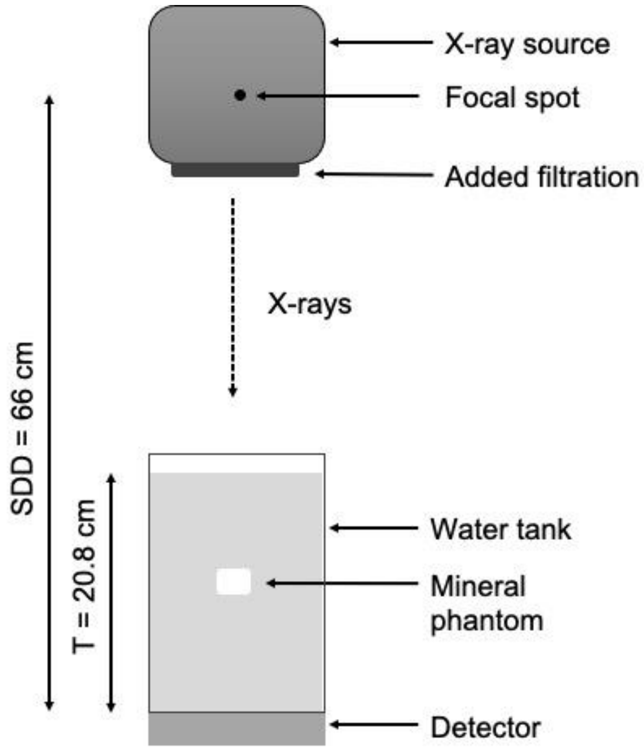

Figure 2. Experimental configuration used for the evaluation of the method.

For the measurement of the detector response curve, the Radcal 2026C ionization chamber was placed at 66 cm from the output of the X-ray tube. The entrance surface air kerma was measured for several tube current-time products. The low-and high-energy images were acquired in 16 bit and regions of interest (ROIs) of 500 × 500 pixels were measured from each low-and high-energy image. The mean pixel value (MPV) and the standard deviation (SD) of each ROI were calculated. The relationship between MPV and detector entrance dose was determined using linear regression, and the corresponding graph is presented in Figure 3.

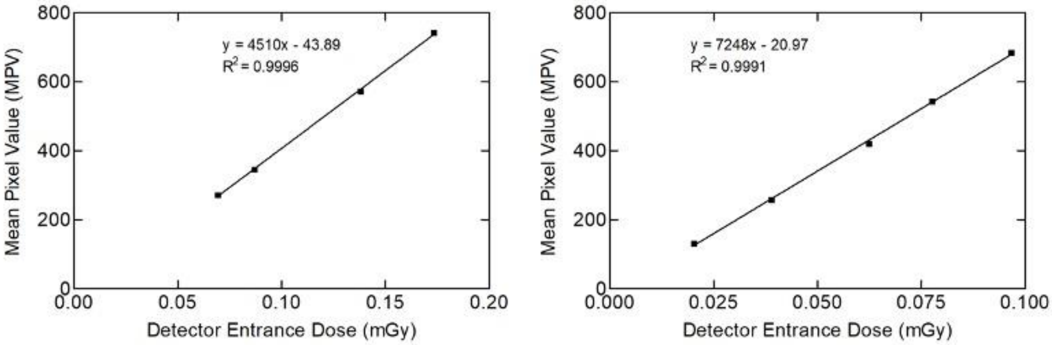

Figure 3. Plot of mean pixel value as a function of the detector entrance dose for the low (**right**)-and high (**left**)-energy.

2.2.2. Phantoms

As was stated earlier, the spotty calcifications found in atherosclerotic plaques are 3 mm or smaller [43,58–60], and although kidney/uteric stones of the same size do not need surgery (pass spontaneously), the knowledge of their composition is important. The 3 mm was set as the highest examined mineral crystal thickness based on the fact that 3 mm is the upper limit for a calcification to be considered as spotty calcification. The discrimination between HAp and either of the two mineral crystal types resulted in lower false positive (%), false negative (%) and overlap area (%) values compared with the discrimintation between $CaCO_3$ and CaC_2O_4. For the experimental evaluation of the method, hydroxyapatite phantoms of 0.7 mm, 1 mm, 1.5 mm and 3 mm thickness were constructed. Phantoms with the equivalent thicknesses of $CaCO_3$ and CaC_2O_4 were also constructed, with hydroxyapatite (FLUKA 21223, ≥90% purity), calcium carbonate (CAS Nr: 207-439-9, ≥99% purity), calcium oxalate (CAS Nr: 563-72-4, 99.99% purity) and epoxy resin ($C_{19}H_{23}ClO_4$) [85]. Each mineral crystal was mixed with the same quantity of epoxy resin and placed into silicon tubes (22.31 mm inner diameter). An epoxy resin phantom, with the same quantity of epoxy used in the mineral mixtures, was constructed and positioned in the beam path when measurements without mineral crystal phantoms were implemented. A vacuum tube VACIOTEM-T (SELECTA, Barcelona, Spain) was used to diminish the remaining air in the phantoms. Each phantom was immersed in a PMMA tank with dimensions of 20 × 20 × 25 cm^3 filled with double distilled water (20.8 cm thickness) to simulate the torso. Figure 4 illustrates the constructed mineral crystal phantoms for the experimental verification.

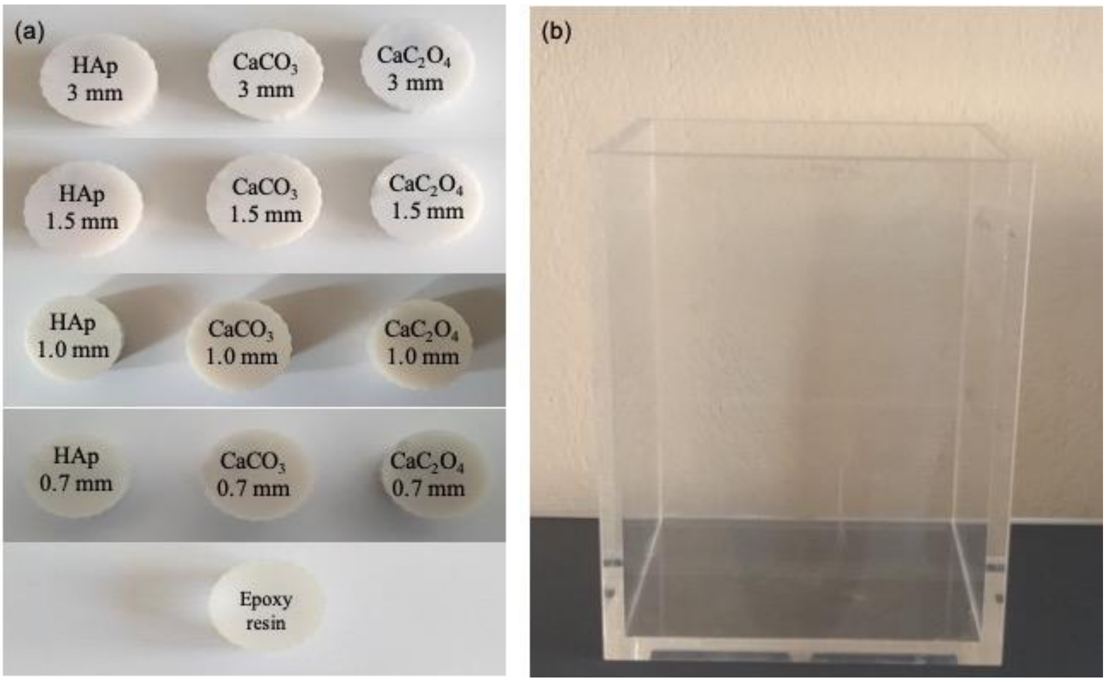

Figure 4. (**a**) Mineral crystal phantoms of (from top to bottom) 3 mm, 1.5 mm, 1.0 mm and 0.7 mm thick HAp and the equivalent thicknesses and the epoxy resin phantom; (**b**) the water tank.

Ten low and ten high-energy images were acquired for each phantom for the determination of the effective m_{Ca}/m_P and the CV ($CV_{m_{Ca}/m_P,experimental}(\%) = SD_{m_{Ca}/m_P}/mean_{m_{Ca}/m_P}$). After every low-and high-energy image combination acquisition, the phantoms were repositioned in order to take into consideration the possible inhomogeneity of the phantoms. Twenty ROIs of 44 × 44 pixels, corresponding to 0.99 × 0.99 mm^2, were obtained in each image as this area is close to the dimensions of kidney/uteric stones or atherosclerotic plaques' calcifications and achieving an adequate number of photons [79]. The MPVs of the ROIs were converted into photon values for the calculation of the effective m_{Ca}/m_P. Figure 5 illustrates indicative low energy images of the 3 mm thick phantoms and the profiles of each phantom image. The graph with the profiles shows that the calcium oxalate and calcium carbonate phantoms with equivalent thicknesses of 3 mm resulted in almost equal photon beam attenuation to the 3 mm hydrohyapatite phantom.

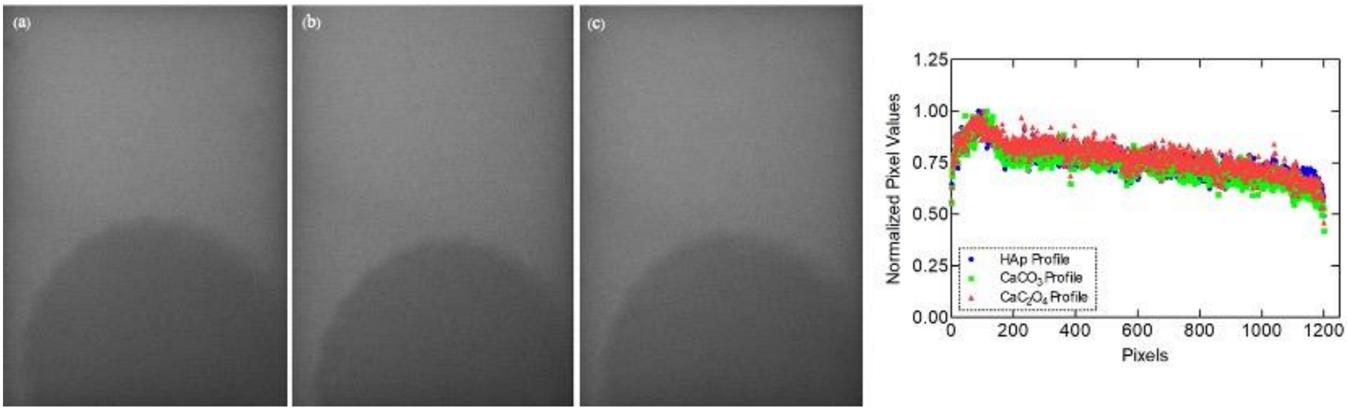

Figure 5. Low energy images of (**a**) 3 mm thick HAp, and the equivalent thicknesses for (**b**) $CaCO_3$ and (**c**) CaC_2O_4 phantoms.

The Cadmium Telluride AMPTEK XR-100T (Amptek, Inc., Bedford, MA, USA) was used to measure the filtered spectra for the low-and high-energy, respectively, and thus the mean pixel values were converted into the number of photons [79,87,102,103]. The spectrophotometer was calibrated for energy scales, linearity checks and energy resolution with the use of ^{125}I and ^{99m}Tc γ-ray calibration sources [101]. The total entrance dose was 8.38 mGy.

In order to assess the experimental results, a statistical analysis was conducted. As the effective m_{Ca}/m_P probability distribution is not Gaussian, the Mann–Whitney U non-parametric statistical test was applied to the measured effective m_{Ca}/m_P values [79]. Through the two-tailed Mann–Whitney U non-parametric statistical test, we investigated if there was a statistically significant difference between the mineral crystal types tested [79,104]. For all tests, the significance level was set at 5%.

3. Results and Discussion

3.1. Simulation Study

3.1.1. Monoenergetic Beams

Figure 6 illustrates the calculated $CV_{m_{Ca}/m_P}(\%)$ for all mineral crystal types examined, as a function of the low- and high-energy combinations, at 5 keV increments. From Figure 6a–c the results for indicative thicknesses of HAp are shown, 1 mm (Figure 6a) to 3 mm (Figure 6c) at 1 mm increments, and the equivalent thicknesses of $CaCO_3$ and CaC_2O_4 are presented in Table 1. In all cases, for low energies ranging from 40 to 50 keV combined with all high energies, the $CV_{m_{Ca}/m_P}(\%)$ ranged from the minimum $CV_{m_{Ca}/m_P}(\%)$ value up to +20% of the minimum.

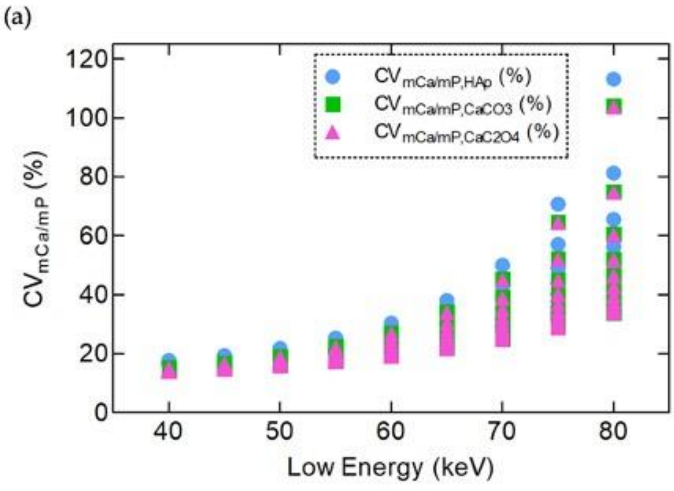

Figure 6. *Cont.*

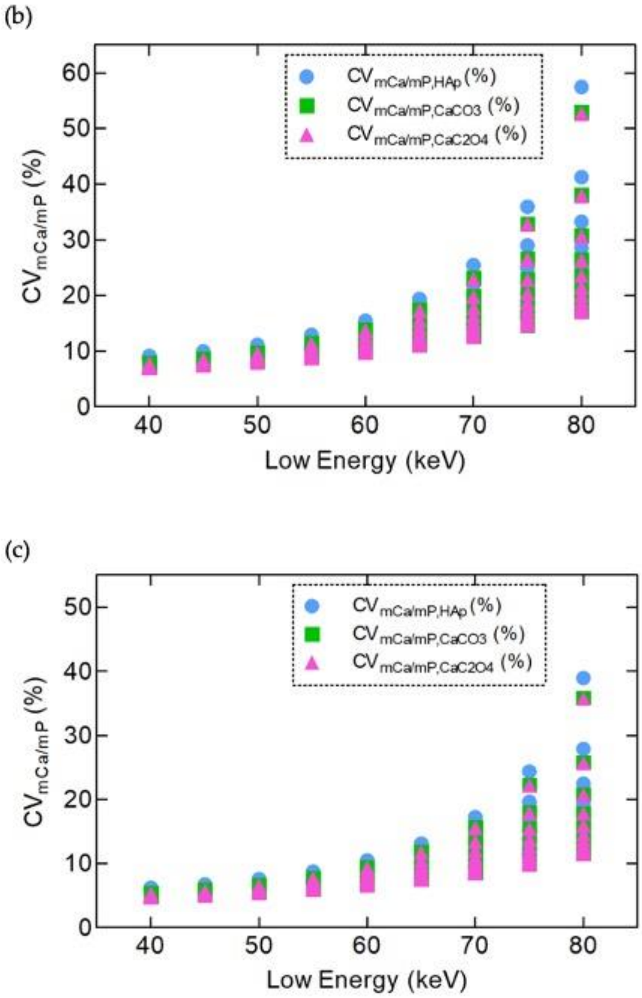

Figure 6. $CV_{m_{Ca}/m_P,HAp}(\%)$, $CV_{m_{Ca}/m_P,CaCO_3}(\%)$, and $CV_{m_{Ca}/m_P,CaC_2O_4}(\%)$ as a function of low- and high-energy combinations for (**a**) 1 mm, (**b**) 2 mm, and (**c**) 3 mm thick HAp and the equivalent thicknesses of $CaCO_3$ and CaC_2O_4.

The effective m_{Ca}/m_P is calculated with the use of a three-equation system. As the low- and high-energy converge, they lead to linear dependency. This results in the increase in the $CV_{m_{Ca}/m_P}(\%)$, which is depicted in Figure 6.

3.1.2. Polyenergetic X-rays

Figure 7 shows the mean energies and photons/mm^2 of the examined filters, as a function of the surface density (g cm^{-2}). Figure 7b illustrates the results for the low energy filters. Although aluminum resulted in lower mean energies compared to the other filters, it provided the highest number of photons through the whole surface density range, which is an important factor for the analytical model. Additionally, aluminum is a low-cost filter commonly used for beam filtration in X-ray systems. Figure 7c,d show that in both mean energy and the number of photons, the high energy filters appeared to be grouped. As in mean energy (Figure 7c), antimony, tin and bismuth resulted in higher mean energies, while chromium and vanadium resulted in lower mean energies. When the aforementioned filters were examined for the number of photons, the results of the groups mentioned above were reversed. Antimony, tin and bismuth resulted in a lower number of photons, while chromium and vanadium resulted in a higher number of photons. Regardless, the examined factors gallium and copper resulted in intermediate values. More specifically, the mean energies of copper and gallium were on average 7.98% lower than chromium and vanadium, while the mean energies of antimony, tin and bismuth were on average

15.55% lower than chromium and vanadium. As for the number of photons, chromium and vanadium resulted in 5.40 times (on average) higher number of photons than copper and vanadium and 38.52 times (on average) higher than antimony, tin and bismuth. Thus, the use of copper or gallium is a good compromise among the factors examined. Since vanadium cannot be found as foil, copper was selected as the high energy filter.

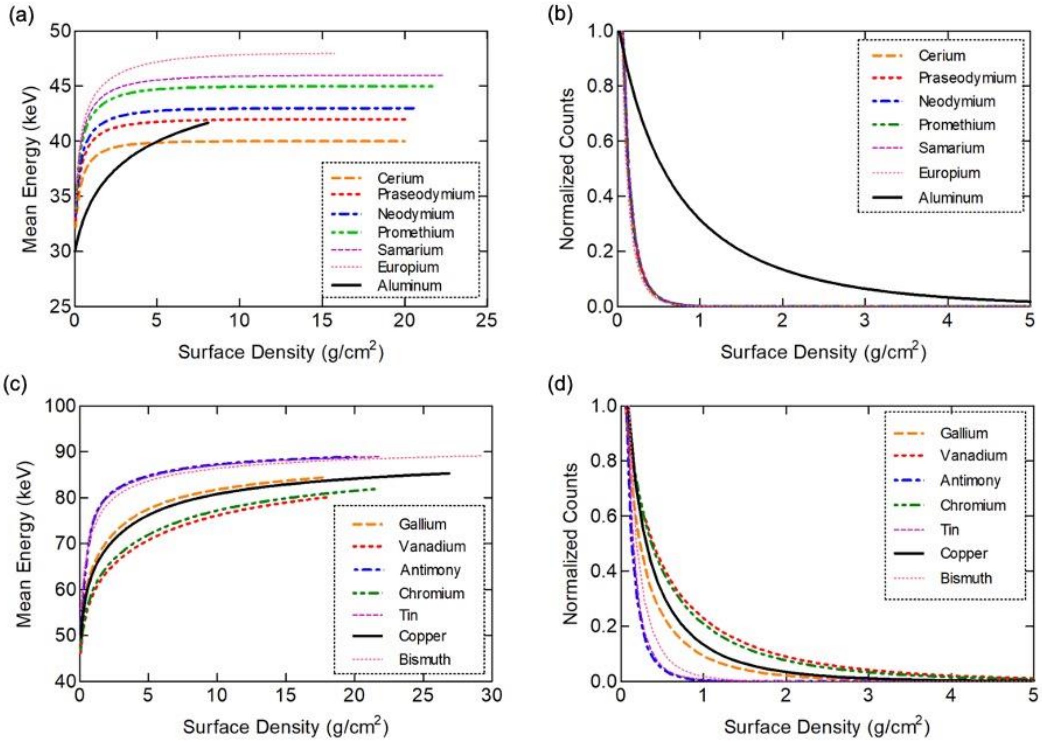

Figure 7. Mean energy (keV) and number of photons (photons mm^{-2}) of filters examined for the low (**a**,**b**)- and high (**c**,**d**)-energy.

A study, based on the nonparametric statistical analysis, was conducted in order to find the proper thicknesses for both aluminum and copper used to modify the X-ray spectra. From all the examined filter thickness combinations, ranging from 0.01 to 3 cm at 0.01 cm increments, the false negative (%), false positive (%) and the overlap area (%) were estimated. Based on the results of this study, the irradiation conditions were the following: (i) for the low energy (50 kVp) images, a 3 mm aluminum filter was applied (inherent filtration), and 3 mm of copper for the high energy (90 kVp) images. This filter thickness combination led to lower false negative (%) and false positive (%) values, and as a result a lower overlap area (%) value. This can be attributed to the fact that both low- and high-energy spectra resulted in an adequate number of photons. Additionally, the aforementioned filter thickness led to spectral separation between the low- and high-energy spectra, which is a key factor for mineral characterization. The mean energies were 34 and 72 keV for the low- and high-energy, respectively.

Table 3 shows the results of the nonparametric statistical analysis for the above irradiation conditions. The false negative (%), false positive (%) and the overlap area (%) are presented for mineral crystal thicknesses ranging from 0.50 to 3.00 mm, at 0.50 mm increments, of hydroxyapatite and the equivalent of calcium carbonate and calcium oxalate. The overlap area is the sum of the false positive and false negative values. For the examined mineral crystal thicknesses, the $CV_{m_{Ca}/m_P,HAp}(\%)$ values were 47.63 and 9.48%, the $CV_{m_{Ca}/m_P,CaCO_3}(\%)$ values were 37.89 and 8.26%, and the $CV_{m_{Ca}/m_P,CaC_2O_4}(\%)$ values were 40.53 and 8.12% for 1.50 and 3.00 mm, respectively.

Table 3. False negative (FN), false positive (FP) and overlap area (OA) values for indicative thicknesses.

Case	HAp Thickness (mm)	FN (%)	FP (%)	OA (%)
HAp; $CaCO_3$	0.50	51.86	35.51	87.37
	1.00	31.57	29.83	61.40
	1.50	24.83	22.94	47.77
	2.00	19.39	18.35	37.73
	2.50	15.62	14.77	30.40
	3.00	13.50	12.52	26.02
HAp; CaC_2O_4	0.50	50.46	32.58	83.04
	1.00	28.01	26.43	54.44
	1.50	20.45	19.30	39.75
	2.00	15.11	14.11	29.21
	2.50	11.40	10.87	22.27
	3.00	8.99	9.04	18.03
$CaCO_3$; CaC_2O_4	0.50	55.35	34.82	90.17
	1.00	45.10	46.43	91.53
	1.50	45.23	43.36	88.59
	2.00	43.48	42.51	85.99
	2.50	41.88	41.53	83.40
	3.00	42.04	40.16	82.20

Regardless of the examined case, the overlap areas corresponding to smaller thicknesses of the mineral crystals were increased compared to higher thicknesses. Additionally, when the case of discrimination between $CaCO_3$ and CaC_2O_4 was investigated, the overlap areas were increased compared to the corresponding HAp; $CaCO_3$ and HAp; CaC_2O_4 cases for all thicknesses.

3.2. Experimental Verification

Table 4 shows the averaged measured effective m_{Ca}/m_P, $CV_{m_{Ca}/m_P,experimental}(\%)$ values and the results of the Mann–Whitney U test for the examined thicknesses. In all cases, the critical U value was 127 [104] since in each phantom image 20 ROIs were selected.

Table 4. Averaged m_{Ca}/m_P for 0.70 mm, 1.00 mm, 1.50 mm and 3.00 mm thick phantoms, $CV_{m_{Ca}/m_P,experimental}(\%)$ and Mann–Whitney U test results.

HAp Thickness (mm)	Averaged Effective m_{Ca}/m_P			$CV_{m_{Ca}/m_P,experimental}$			Mann–Whitney U Test			
							U Value			
	HAp	$CaCO_3$	CaC_2O_4	HAp	$CaCO_3$	CaC_2O_4	HAp; $CaCO_3$	HAp; CaC_2O_4	$CaCO_3$; CaC_2O_4	Critical Value
0.70	2.12	1.70	1.59	72.46	53.89	50.02	75	62	142	127
1.00	2.13	1.73	1.62	51.76	36.91	32.44	38	23	131	127
1.50	2.13	1.73	1.62	32.35	25.28	26.03	0	0	120	127
3.00	2.29	1.73	1.64	19.79	17.32	18.22	0	0	115	127

Based on the results shown in Table 4, there are statistically significant differences ($p < 0.05$) between the mineral crystals examined for thicknesses of 0.70 mm or higher for HAp; $CaCO_3$ and HAp; CaC_2O_4 cases. The $CV_{m_{Ca}/m_P,experimental}(\%)$ values of all mineral crystals were found to be higher than the ones calculated in the simulation study. This can be attributed to the fact that the effective mass attenuation coefficients were used instead of the mass attenuation coefficients, due to the fact that the neighboring energy pairs that result in linear dependence of the equation system are not taken into consideration. Additionally, in the determination of the effective mass attenuation coefficients, the effect of beam hardening is not considered [74]. Finally, the instability of both the electronics and the X-ray tube was an additional factor to the above that contributed to the $CV_{m_{Ca}/m_P,experimental}(\%)$ value increase.

The proposed dual energy method characterizes mineral crystals of 0.70 mm thick or higher, found in kidney/uteric stones and calcifications in atherosclerotic plaques. The statistical noise that has an impact on the number of photons finally detected was the main reason for the increase in the $CV_{m_{Ca}/m_P,experimental}(\%)$ value and the higher U values in the case of $CaCO_3$; CaC_2O_4. The latter case was proved to be the most difficult among the three cases examined. Since $CaCO_3$ is rarely found in kidney/uteric stones [23,29,30] and CaC_2O_4 and hydroxyapatite are the main calcium mineral crystals found in atherosclerotic plaques [42,43,45–55], the results indicate that the mainly found mineral crystals' characterization can be accomplished by the proposed method.

The discrimination of calcifications smaller than 3.00 mm (spotty calcifications) is of great importance. Apart from the fact that calcifications are clinical indicator for plaques' instability [43,44,49,58–66], the presence of hydroxyapatite increases the possibility of rapture. The results of this work are also important for patients diagnosed with urolithiasis or nephrolithiasis. Despite the fact that kidney/uteric stones smaller than 3.00 mm, such as the ones examined in this work, do not need surgery, the knowledge of their composition will assist the physician to plan a better treatment for the patient and may prevent surgery [3,9–17].

The results presented above, for both simulation study and experimental verifications, can be improved by increasing the entrance dose without risking the patients' health. The low energy irradiation could guide the physician to identify and locate the kidney/uteric stones or atherosclerotic plaques' calcifications, while the high energy irradiation can be restricted to a smaller area including only the stones or calcifications. As it has already been mentioned, the total entrance dose was 8.38 mGy, resulting in 0.22 mSv and 3.84 mSv effective equivalent doses for urolithiasis/nephrolithiasis and atherosclerotic plaques, respectively. Previous studies for discrimination between different mineral crystal types found in kidney/uteric stones using CT resulted in an entrance dose of 10 mGy and an effective dose of 8 up to 10 mSv [105–109]. When DECT was used in phantom studies, the entrance dose ranged from 6 to 26.2 mGy and 8.2 to 14.6 mGy when patients were involved [10,110–113]. Low dose (LDCT) and ultra-low dose CT (ULDCT) were also used, resulting in an absorbed dose of 3 mSv or less [105,107–109,114]. In all cases, there were difficulties in discrimination between mineral crystals when the stones were 3.00 mm or smaller, and especially when LDCT and ULDCT were used [105,107–109,114]. As for atherosclerotic plaques, the effective dose of CT ranges from 5.4 to 8 mSv, while the typical entrance dose for DECT is 19 mGy and 23 mGy for the low- and high-energy, respectively [71,115–118].

The radiation field that was used in order to obtain the low- and high-energy images was almost equal to the dimensions of the CMOS detector (27×36 mm^2) of the DE system. Although the radiation field's dimensions are small, the scatter radiation still exists but in a smaller amount compared to that of usual radiation fields used in radiography. When the kidney/uteric stones or atherosclerotic plaques' calcifications are identified in a radiographic image, the field will be even smaller so only the kidney/uteric stones or atherosclerotic plaques' calcifications will be irradiated.

In order to achieve an adequate photon flux, especially in the high energy where a 3 mm Cu filter is applied, the time-current product was increased to 400 mAs. The results of the proposed method will be further improved if a specialized X-ray system is used to preserve a higher photon flux. As it is already mentioned, apart from the adequate number of photons, spectral separation is also an important parameter which improves mineral characterization. An X-ray system with higher photon flux and thicker filters will further improve the spectral separation. In future work, a more realistic torso phantom will be constructed in order to further evaluate the method, and Monte Carlo methods or convolution kernel-based approaches will be adopted for scatter correction [118–121].

4. Conclusions

In this work, a dual energy method was proposed for the discrimination of mineral crystals found in kidney/uteric stones and calcifications in atherosclerotic plaques through the effective m_{Ca}/m_P. The potential of the method to differentiate HAp, $CaCO_3$ and CaC_2O_4 was investigated using both simulations (monoenergetic and polyenergetic X-ray beams) and experimental verification. The experimental results revealed that with the proposed method, the mineral crystals can be characterized for thicknesses of 0.70 mm or higher for HAp; $CaCO_3$ and HAp; CaC_2O_4 cases. Further studies will show if the proposed method can provide in vivo information for the mineral crystals.

Author Contributions: Conceptualization, N.M. and V.K.; methodology, N.M., V.K. and G.F.; software, N.M. and V.K.; validation, N.M., V.K., C.M. and G.F.; formal analysis, N.M., V.K. and G.F.; investigation, N.M., V.K., C.M. and G.F.; resources, N.M. and V.K.; data curation, N.M., V.K. and G.F.; writing—original draft preparation, N.M. and V.K.; writing—review and editing, N.M., V.K., C.M. and G.F.; visualization, G.F.; supervision, G.F.; project administration, C.M. and G.F.; funding acquisition, C.M. and G.F. All authors have read and agreed to the published version of the manuscript.

Funding: This research is co-financed by Greece and the European Union (European Social Fund-ESF) through the Operational Programme «Human Resources Development, Education and Lifelong Learning 2014–2020» in the context of the project "Human body mineral characterization using Dual Energy X-ray method" (MIS 5050326). The APC was funded by the Special Account for Research Grants, of the University of West Attica, Greece.

Data Availability Statement: Data are contained within the article.

Conflicts of Interest: The authors declare no conflict of interest.

References

1. Scales, C.D.; Saigal, C.S.; Hanley, J.M.; Dick, A.W.; Setodji, C.M.; Litwin, M.S.; NIDDK Urologic Diseases in America Project. The impact of unplanned post procedure visits in the management of patients with urinary stones. *Surgery* **2014**, *155*, 769–775. [CrossRef]
2. Saigal, C.S.; Joyce, G.; Timilsina, A.R.; Urologic Diseases in America Project. Direct and indirect costs of nephrolithiasis in an employed population: Opportunity for disease management? *Kidney Int.* **2005**, *68*, 1808–1814. [CrossRef]
3. Jendeberg, J.; Geijer, H.; Alshamari, M.; Cierzniak, B.; Lidén, M. Size matters: The width and location of a ureteral stone accurately predict the chance of spontaneous passage. *Eur. Radiol.* **2017**, *27*, 4775–4785. [CrossRef]
4. Parmar, M.S. Kidney Stones. *BMJ* **2004**, *328*, 1420–1424. [CrossRef]
5. Sandegard, E. Prognosis of stone in the ureter. *Acta Chir. Scand. Suppl.* **1956**, *219*, 1–67. [PubMed]
6. Ueno, A.; Kawamura, T.; Ogawa, A.; Takayasu, H. Relation of spontaneous passage of ureteral calculi to size. *Urology* **1977**, *10*, 544–546. [CrossRef]
7. Coll, D.M.; Varanelli, M.J.; Smith, R.C. Relationship of Spontaneous Passage of Ureteral Calculi to Stone Size and Location as Revealed by Unenhanced Helical CT. *Am. J. Roentgenol.* **2002**, *178*, 101–103. [CrossRef] [PubMed]
8. Simon, J.C.; Maxwell, A.D.; Bailey, M.R. Some Work on the Diagnosis and Management of Kidney Stones with Ultra-sound. *Acoust. Today* **2017**, *13*, 52–59.
9. Eliahou, R.; Hidas, G.; Duvdevani, M.; Sosna, J. Determination of Renal Stone Composition with Dual-Energy Computed Tomography: An Emerging Application. *Semin. Ultrasound CT MRI* **2010**, *31*, 315–320. [CrossRef]
10. Qu, M.; Ramirez-Giraldo, J.C.; Leng, S.; Williams, J.C.; Vrtiska, T.J.; Lieske, J.C.; McCollough, C.H. Dual-Energy Dual-Source CT With Additional Spectral Filtration Can Improve the Differentiation of Non–Uric Acid Renal Stones: An Ex Vivo Phantom Study. *Am. J. Roentgenol.* **2011**, *196*, 1279–1287. [CrossRef] [PubMed]
11. Kourambas, J.; Aslan, P.; Teh, C.L.; Mathias, B.J.; Preminger, G.M. Role of Stone Analysis in Metabolic Evaluation and Medical Treatment of Nephrolithiasis. *J. Endourol.* **2001**, *15*, 181–186. [CrossRef] [PubMed]
12. Pak, C.Y.; Poindexter, J.R.; Adams-Huet, B.; Pearle, M.S. Predictive value of kidney stone composition in the detection of metabolic abnormalities. *Am. J. Med.* **2003**, *115*, 26–32. [CrossRef]
13. Zilberman, D.; Ferrandino, M.; Preminger, G.; Paulson, E.; Lipkin, M.; Boll, D. In Vivo Determination of Urinary Stone Composition Using Dual Energy Computerized Tomography With Advanced Post-Acquisition Processing. *J. Urol.* **2010**, *184*, 2354–2359. [CrossRef] [PubMed]
14. Li, X.-H.; Zhao, R.; Liu, B.; Yu, Y.-Q. Determination of urinary stone composition using dual-energy spectral CT: Initial in vitro analysis. *Clin. Radiol.* **2013**, *68*, e370–e377. [CrossRef] [PubMed]
15. Wisenbaugh, E.S.; Paden, R.G.; Silva, A.C.; Humphreys, M.R. Dual-energy vs Conventional Computed Tomography in Determining Stone Composition. *Urology* **2014**, *83*, 1243–1247. [CrossRef] [PubMed]

16. Zisman, A.L. Effectiveness of Treatment Modalities on Kidney Stone Recurrence. *Clin. J. Am. Soc. Nephrol.* **2017**, *12*, 1699–1708. [CrossRef] [PubMed]
17. Wood, B.G.; Urban, M.W. Detecting Kidney Stones Using Twinkling Artifacts: Survey of Kidney Stones with Varying Composition and Size. *Ultrasound Med. Biol.* **2020**, *46*, 156–166. [CrossRef]
18. Macfarlane, M.T. *Urology*, 5th ed.; Lippincott William & Wilkins: Baltimore, MD, USA, 2015; pp. 132–133.
19. Primak, A.N.; Fletcher, J.G.; Vrtiska, T.J.; Dzyubak, O.P.; Lieske, J.C.; Jackson, M.E.; Williams, J.C.; McCollough, C.H. Noninvasive Differentiation of Uric Acid versus Non–Uric Acid Kidney Stones Using Dual-Energy CT. *Acad. Radiol.* **2007**, *14*, 1441–1447. [CrossRef] [PubMed]
20. Basiri, A.; Taheri, M.; Taheri, F. What is the state of the stone analysis techniques in urolithiasis? *Urol. J.* **2012**, *9*, 445–454.
21. Evan, A.P.; Worcester, E.M.; Coe, F.L.; Williams, J.; Lingeman, J.E. Mechanisms of human kidney stone formation. *Urolithiasis* **2014**, *43*, 19–32. [CrossRef]
22. Sethmann, I.; Grohé, B.; Kleebe, H.-J. Replacement of hydroxylapatite by whewellite: Implications for kidney-stone formation. *Miner. Mag.* **2014**, *78*, 91–100. [CrossRef]
23. Keshavarzi, B.; Ashayeri, N.Y.; Moore, F.; Irani, D.; Asadi, S.; Zarasvandi, A.; Salari, M. Mineralogical Composition of Urinary Stones and Their Frequency in Patients: Relationship to Gender and Age. *Minerals* **2016**, *6*, 131. [CrossRef]
24. Vásquez-Quitral, P.; Arana, J.T.; Miras, M.C.; Acevedo, D.F.; Barbero, C.A.; Neira-Carrillo, A. Effect of Diazotated Sulphonated Polystyrene Films on the Calcium Oxalate Crystallization. *Crystals* **2017**, *7*, 70. [CrossRef]
25. Grant, C.M.; Guzman, G.; Stainback, R.P.; Amdur, R.L.; Mufarrij, P.W.; Guzman, G. Variation in Kidney Stone Composition Within the United States. *J. Endourol.* **2018**, *32*, 973–977. [CrossRef] [PubMed]
26. Letavernier, E.; Bouderlique, E.; Zaworski, J.; Martin, L.; Daudon, M. Pseudoxanthoma Elasticum, Kidney Stones and Pyrophosphate: From a Rare Disease to Urolithiasis and Vascular Calcifications. *Int. J. Mol. Sci.* **2019**, *20*, 6353. [CrossRef] [PubMed]
27. Chen, S.-J.; Chiu, K.-Y.; Chen, H.-Y.; Lin, W.-Y.; Chen, Y.-H.; Chen, W.-C. Animal Models for Studying Stone Disease. *Diagnostics* **2020**, *10*, 490. [CrossRef] [PubMed]
28. Bargagli, M.; Tio, M.C.; Waikar, S.S.; Ferraro, P.M. Dietary Oxalate Intake and Kidney Outcomes. *Nutrients* **2020**, *12*, 2673. [CrossRef]
29. Daudon, M.; Hennequin, C.; Lacour, B.; Le Moël, G.; Donsimoni, R.; Fellahi, S.; Paris, M.; Troupel, S. Sex- and age-related composition of 10,617 calculi analyzed by infrared spectroscopy. *Urol. Res.* **1995**, *23*, 319–326. [CrossRef]
30. Frochot, V.; Castiglione, V.; Lucas, I.T.; Haymann, J.-P.; Letavernier, E.; Bazin, D.; Fogazzi, G.B.; Daudon, M. Advances in the identification of calcium carbonate urinary crystals. *Clin. Chim. Acta* **2021**, *515*, 1–4. [CrossRef] [PubMed]
31. Zarse, C.A.; McAteer, J.A.; Tann, M.; Sommer, A.J.; Kim, S.C.; Paterson, R.F.; Hatt, E.K.; Lingeman, J.E.; Evan, A.P.; Williams, J.C. Helical computed tomography accurately reports urinary stone composition using attenuation values: In vitro verification using high-resolution micro-computed tomography calibrated to fourier transform infrared microspectroscopy. *Urology* **2004**, *63*, 828–833. [CrossRef]
32. Mitcheson, H.D.; Zamenhof, R.G.; Bankoff, M.S.; Prien, E.L. Determination of the Chemical Composition of Urinary Calculi by Computerized Tomography. *J. Urol.* **1983**, *130*, 814–819. [CrossRef]
33. Jia, H.; Abtahian, F.; Aguirre, A.D.; Lee, S.; Chia, S.; Lowe, H.; Kato, K.; Yonetsu, T.; Vergallo, R.; Hu, S.; et al. In Vivo Diagnosis of Plaque Erosion and Calcified Nodule in Patients With Acute Coronary Syndrome by Intravascular Optical Coherence Tomography. *J. Am. Coll. Cardiol.* **2013**, *62*, 1748–1758. [CrossRef]
34. Yahagi, K.; Davis, H.R.; Arbustini, E.; Virmani, R. Sex differences in coronary artery disease: Pathological observations. *Atherosclerosis* **2015**, *239*, 260–267. [CrossRef]
35. Spagnoli, L.G.; Mauriello, A.; Sangiorgi, G.; Fratoni, S.; Bonanno, E.; Schwartz, R.S.; Piepgras, D.G.; Pistolese, R.; Ippoliti, A.; Holmes, D.R. Extracranial Thrombotically Active Carotid Plaque as a Risk Factor for Ischemic Stroke. *JAMA* **2004**, *292*, 1845–1852. [CrossRef]
36. Virmani, R.; Burke, A.P.; Farb, A.; Kolodgie, F.D. Pathology of the Vulnerable Plaque. *J. Am. Coll. Cardiol.* **2006**, *47*, C13–C18. [CrossRef] [PubMed]
37. Barrett, H.E.; Van der Heiden, K.; Farrell, E.; Gijsen, F.J.; Akyildiz, A.C. Calcifications in atherosclerotic plaques and impact on plaque biomechanics. *J. Biomech.* **2019**, *87*, 1–12. [CrossRef] [PubMed]
38. Adamson, P.D.; Vesey, A.T.; Joshi, N.V.; Newby, D.E.; Dweck, M.R. Salt in the wound: 18F-fluoride positron emission tomography for identification of vulnerable coronary plaques. *Cardiovasc. Diagn. Ther.* **2015**, *5*, 150–155. [CrossRef] [PubMed]
39. O'Brien, K.D.; Kuusisto, J.; Reichenbach, D.D.; Ferguson, M.; Giachelli, C.; Alpers, C.E.; Otto, C.M. Osteopontin Is Expressed in Human Aortic Valvular Lesions. *Circulation* **1995**, *92*, 2163–2168. [CrossRef] [PubMed]
40. Chen, W.; Dilsizian, V. Targeted PET/CT Imaging of Vulnerable Atherosclerotic Plaques: Microcalcification with Sodium Fluoride and Inflammation with Fluorodeoxyglucose. *Curr. Cardiol. Rep.* **2013**, *15*, 364. [CrossRef] [PubMed]
41. New, S.E.P.; Goettsch, C.; Aikawa, M.; Marchini, J.F.; Shibasaki, M.; Yabusaki, K.; Libby, P.; Shanahan, C.M.; Croce, K.; Aikawa, E. Macrophage-Derived Matrix Vesicles: An Alternative Novel Mechanism for Microcalcification in Athero-sclerotic Plaques. *Circ. Res.* **2013**, *113*, 72–77. [CrossRef] [PubMed]
42. Creager, M.D.; Hohl, T.; Hutcheson, J.D.; Moss, A.J.; Schlotter, F.; Blaser, M.C.; Park, M.-A.; Lee, L.H.; Singh, S.A.; Alcaide-Corral, C.J.; et al. 18F-Fluoride Signal Amplification Identifies Microcalcifications Associated With Atherosclerotic Plaque Instability in Positron Emission Tomography/Computed Tomography Images. *Circ. Cardiovasc. Imaging* **2019**, *12*, e007835. [CrossRef]

43. Shi, X.; Gao, J.; Lv, Q.; Cai, H.; Wang, F.; Ye, R.; Liu, X. Calcification in Atherosclerotic Plaque Vulnerability: Friend or Foe? *Front. Physiol.* **2020**, *11*, 56. [CrossRef]
44. Sakaguchi, M.; Hasegawa, T.; Ehara, S.; Matsumoto, K.; Mizutani, K.; Iguchi, T.; Ishii, H.; Nakagawa, M.; Shimada, K.; Yoshiyama, M. New insights into spotty calcification and plaque rupture in acute coronary syndrome: An optical coherence tomography study. *Heart Vessel.* **2016**, *31*, 1915–1922. [CrossRef] [PubMed]
45. Li, L.; Li, X.; Jia, Y.; Fan, J.; Wang, H.; Fan, C.; Wu, L.; Si, X.; Hao, X.; Wu, P.; et al. Sodium-fluoride PET-CT for the non-invasive evaluation of coronary plaques in symptomatic patients with coronary artery disease: A cross-correlation study with intravascular ultrasound. *Eur. J. Nucl. Med. Mol. Imaging* **2018**, *45*, 2181–2189. [CrossRef]
46. Becker, A.; Epple, M.; Müller, K.; Schmitz, I. A comparative study of clinically well-characterized human atherosclerotic plaques with histological, chemical, and ultrastructural methods. *J. Inorg. Biochem.* **2004**, *98*, 2032–2038. [CrossRef]
47. Kim, K.M. Calcification of matrix vesicles in human aortic valve and aortic media. *Fed. Proc.* **1976**, *35*, 156–162.
48. Schmid, K.; McSharry, W.O.; Pameijer, C.H.; Binette, J. Chemical and physicochemical studies on the mineral deposits of the human atherosclerotic aorta. *Atherosclerosis* **1980**, *37*, 199–210. [CrossRef]
49. Ewence, A.E.; Bootman, M.; Roderick, H.L.; Skepper, J.N.; McCarthy, G.; Epple, M.; Neumann, M.; Shanahan, C.M.; Proudfoot, D. Calcium Phosphate Crystals Induce Cell Death in Human Vascular Smooth Muscle Cells: A Potential Mechanism in Atherosclerotic Plaque Destabilization. *Circ. Res.* **2008**, *103*, e28–e34. [CrossRef] [PubMed]
50. Perrotta, I.; Perri, E. Ultrastructural, Elemental and Mineralogical Analysis of Vascular Calcification in Atherosclerosis. *Microsc. Microanal.* **2017**, *23*, 1030–1039. [CrossRef]
51. Viegas, C.; Araújo, N.; Marreiros, C.; Simes, D. The interplay between mineral metabolism, vascular calcification and inflammation in Chronic Kidney Disease (CKD): Challenging old concepts with new facts. *Aging* **2019**, *11*, 4274–4299. [CrossRef]
52. Jinnouchi, H.; Sato, Y.; Sakamoto, A.; Cornelissen, A.; Mori, M.; Kawakami, R.; Gadhoke, N.V.; Kolodgie, F.D.; Virmani, R.; Finn, A.V. Calcium deposition within coronary atherosclerotic lesion: Implications for plaque stability. *Atherosclerosis* **2020**, *306*, 85–95. [CrossRef]
53. Florea, A.; Sigl, J.; Morgenroth, A.; Vogg, A.; Sahnoun, S.; Winz, O.; Bucerius, J.; Schurgers, L.; Mottaghy, F. Sodium [^{18}F]Fluoride PET Can Efficiently Monitor In Vivo Atherosclerotic Plaque Calcification Progression and Treatment. *Cells* **2021**, *10*, 275. [CrossRef] [PubMed]
54. Herrmann, J.; Babic, M.; Tölle, M.; Van Der Giet, M.; Schuchardt, M. Research Models for Studying Vascular Calcification. *Int. J. Mol. Sci.* **2020**, *21*, 2204. [CrossRef]
55. Myung, S.-K.; Kim, H.-B.; Lee, Y.-J.; Choi, Y.-J.; Oh, S.-W. Calcium Supplements and Risk of Cardiovascular Disease: A Meta-Analysis of Clinical Trials. *Nutrients* **2021**, *13*, 368. [CrossRef] [PubMed]
56. Fishbein, G.A.; Micheletti, R.G.; Currier, J.S.; Singer, E.; Fishbein, M.C. Atherosclerotic oxalosis in coronary arteries. *Cardiovasc. Pathol.* **2008**, *17*, 117–123. [CrossRef] [PubMed]
57. Bischetti, S.; Scimeca, M.; Bonanno, E.; Federici, M.; Anemona, L.; Menghini, R.; Casella, S.; Cardellini, M.; Ippoliti, A.; Mauriello, A. Carotid plaque instability is not related to quantity but to elemental composition of calcification. *Nutr. Metab. Cardiovasc. Dis.* **2017**, *27*, 768–774. [CrossRef] [PubMed]
58. Motoyama, S.; Kondo, T.; Sarai, M.; Sugiura, A.; Harigaya, H.; Sato, T.; Inoue, K.; Okumura, M.; Ishii, J.; Anno, H.; et al. Multislice Computed Tomographic Characteristics of Coronary Lesions in Acute Coronary Syndromes. *J. Am. Coll. Cardiol.* **2007**, *50*, 319–326. [CrossRef]
59. Pflederer, T.; Marwan, M.; Schepis, T.; Ropers, D.; Seltmann, M.; Muschiol, G.; Daniel, W.G.; Achenbach, S. Characterization of culprit lesions in acute coronary syndromes using coronary dual-source CT angiography. *Atherosclerosis* **2010**, *211*, 437–444. [CrossRef]
60. Feuchtner, G.M.; Barbieri, F.; Langer, C.; Beyer, C.; Widmann, G.; Friedrich, G.J.; Cartes-Zumelzu, F.; Plank, F. Non obstructive high-risk plaque but not calcified by coronary CTA, and the G-score predict ischemia. *J. Cardiovasc. Comput. Tomogr.* **2019**, *13*, 305–314. [CrossRef]
61. Kataoka, Y.; Wolski, K.; Uno, K.; Puri, R.; Tuzcu, E.M.; Nissen, S.E.; Nicholls, S.J. Spotty Calcification as a Marker of Accelerated Progression of Coronary Atherosclerosis: Insights From Serial Intravascular Ultrasound. *J. Am. Coll. Cardiol.* **2012**, *59*, 1592–1597. [CrossRef] [PubMed]
62. Stefanadis, C.; Antoniou, C.; Tsiachris, D.; Pietri, P. Coronary Atherosclerotic Vulnerable Plaque: Current Perspectives. *J. Am. Hear. Assoc.* **2017**, *6*, e005543. [CrossRef]
63. Nishizawa, Y.; Higuchi, C.; Nakaoka, T.; Omori, H.; Ogawa, T.; Sakura, H.; Nitta, K. Compositional Analysis of Coronary Artery Calcification in Dialysis Patients in vivo by Dual-Energy Computed Tomography Angiography. *Ther. Apher. Dial.* **2018**, *22*, 365–370. [CrossRef] [PubMed]
64. Mizukoshi, M.; Kubo, T.; Takarada, S.; Kitabata, H.; Ino, Y.; Tanimoto, T.; Komukai, K.; Tanaka, A.; Imanishi, T.; Akasaka, T. Coronary Superficial and Spotty Calcium Deposits in Culprit Coronary Lesions of Acute Coronary Syndrome as Determined by Optical Coherence Tomography. *Am. J. Cardiol.* **2013**, *112*, 34–40. [CrossRef] [PubMed]
65. Ong, D.S.; Lee, J.S.; Soeda, T.; Higuma, T.; Minami, Y.; Wang, Z.; Lee, H.; Yokoyama, H.; Yokota, T.; Okumura, K.; et al. Coronary Calcification and Plaque Vulnerability. *Circ. Cardiovasc. Imaging* **2016**, *9*, 003929. [CrossRef] [PubMed]
66. Mori, H.; Torii, S.; Kutyna, M.; Sakamoto, A.; Finn, A.V.; Virmani, R. Coronary Artery Calcification and its Progression: What Does It Really Mean? *JACC Cardiovasc. Imaging* **2018**, *11*, 127–142. [CrossRef]

67. Barreto, M.; Schoenhagen, P.; Nair, A.; Amatangelo, S.; Milite, M.; Obuchowski, N.A.; Lieber, M.L.; Halliburton, S.S. Potential of dual-energy computed tomography to characterize atherosclerotic plaque: Ex vivo assessment of human coronary arteries in comparison to histology. *J. Cardiovasc. Comput. Tomogr.* **2008**, *2*, 234–242. [CrossRef] [PubMed]
68. Boll, D.T.; Merkle, E.M.; Paulson, E.K.; Mirza, R.A.; Fleiter, T.R. Calcified Vascular Plaque Specimens: Assessment with Cardiac Dual-Energy Multidetector CT in Anthropomorphically Moving Heart Phantom. *Radiology* **2008**, *249*, 119–126. [CrossRef]
69. Henzler, T.; Porubsky, S.; Kayed, H.; Harder, N.; Krissak, U.R.; Meyer, M.; Sueselbeck, T.; Marx, A.; Michaely, H.; Schoepf, U.J.; et al. Attenuation-based characterization of coronary atherosclerotic plaque: Comparison of dual source and dual energy CT with single-source CT and histopathology. *Eur. J. Radiol.* **2011**, *80*, 54–59. [CrossRef]
70. Nakajima, S.; Ito, H.; Mitsuhashi, T.; Kubo, Y.; Matsui, K.; Tanaka, I.; Fukui, R.; Omori, H.; Nakaoka, T.; Sakura, H.; et al. Clinical application of effective atomic number for classifying non-calcified coronary plaques by dual-energy computed tomography. *Atherosclerosis* **2017**, *261*, 138–143. [CrossRef]
71. Ding, H.; Wang, C.; Malkasian, S.; Johnson, T.; Molloi, S. Characterization of arterial plaque composition with dual energy computed tomography: A simulation study. *Int. J. Cardiovasc. Imaging* **2021**, *37*, 331–341. [CrossRef]
72. Alexander, R.T.; Hemmelgarn, B.R.; Wiebe, N.; Bello, A.; Samuel, S.; Klarenbach, S.W.; Curhan, G.C.; Tonelli, M. Kidney Stones and Cardiovascular Events: A Cohort Study. *Clin. J. Am. Soc. Nephrol.* **2013**, *9*, 506–512. [CrossRef]
73. Devarajan, A. Cross-talk between renal lithogenesis and atherosclerosis: An unveiled link between kidney stone formation and cardiovascular diseases. *Clin. Sci.* **2018**, *132*, 615–626. [CrossRef]
74. Ferraro, P.M.; Taylor, E.N.; Eisner, B.H.; Gambaro, G.; Rimm, E.B.; Mukamal, K.J.; Curhan, G.C. History of Kidney Stones and the Risk of Coronary Heart Disease. *JAMA* **2013**, *310*, 408–415. [CrossRef]
75. Aydin, H.; Yencilek, F.; Erihan, I.B.; Okan, B.; Sarica, K. Increased 10-year cardiovascular disease and mortality risk scores in asymptomatic patients with calcium oxalate urolithiasis. *Urol. Res.* **2011**, *39*, 451–458. [CrossRef]
76. Huang, H.S.; Liao, P.C.; Liu, C.J. Calcium Kidney Stones are Associated with Increased Risk of Carotid Atherosclerosis: The Link between Urinary Stone Risks, Carotid Intima-Media Thickness, and Oxidative Stress Markers. *J. Clin. Med.* **2020**, *9*, 729. [CrossRef]
77. Luo, W.; Zhou, Y.; Gao, C.; Yan, P.; Xu, L. Urolithiasis, Independent of Uric Acid, Increased Risk of Coronary Artery and Carotid Atherosclerosis: A Meta-Analysis of Observational Studies. *BioMed Res. Int.* **2020**, *2020*, 1–11. Available online: https://www.hindawi.com/journals/bmri/2020/1026240/ (accessed on 25 February 2021). [CrossRef]
78. Arafa, A.; Eshak, E.S.; Iso, H. Oxalates, urinary stones and risk of cardiovascular diseases. *Med. Hypotheses* **2020**, *137*, 109570. [CrossRef]
79. Martini, N.; Koukou, V.; Fountos, G.; Michail, C.; Bakas, A.; Kandarakis, I.; Speller, R.; Nikiforidis, G. Characterization of breast calcification types using dual energy x-ray method. *Phys. Med. Biol.* **2017**, *62*, 7741–7764. [CrossRef] [PubMed]
80. Martini, N.; Koukou, V.; Michail, C.; Fountos, G. Dual Energy X-ray Methods for the Characterization, Quantification and Imaging of Calcification Minerals and Masses in Breast. *Crystals* **2020**, *10*, 198. [CrossRef]
81. Keppler, U.; Menges, V. Differences in microcalcification in breast tumors. *Virchows Arch. A Path. Anat. Histol.* **1981**, *393*, 307–313. [CrossRef]
82. Frappart, L.; Rémy, I.; Lin, H.C.; Bremond, A.; Raudrant, D.; Grousson, B.; Vauzelle, J.L. Different types of microcalcifications observed in breast pathology. *Vichows Arch. A Pathol. Anat.* **1987**, *410*, 179–187. [CrossRef]
83. Haka, A.S.; Shafer-Peltier, K.E.; Fitzmaurice, M.; Crowe, J.; Dasari, R.R.; Feld, M.S. Identifying Microcalcifications in Benign and Malignant Breast Lesions by Probing Differences in Their Chemical Composition Using Raman Spectros-copy. *Cancer Res.* **2002**, *62*, 5375–5380.
84. Fandos-Morera, A.; Prats-Esteve, M.; Tura-Soteras, J.M.; Traveria-Cros, A. Breast tumors: Composition of microcalcifications. *Radiology* **1988**, *169*, 325–327. [CrossRef] [PubMed]
85. Baker, R.; Matousek, P.; Ronayne, K.L.; Parker, A.W.; Rogers, K.; Stone, N. Depth profiling of calcifications in breast tissue using picosecond Kerr-gated Raman spectroscopy. *Analyst* **2007**, *132*, 48–53. [CrossRef] [PubMed]
86. Koukou, V.; Martini, N.; Fountos, G.; Michail, C.; Sotiropoulou, P.; Bakas, A.; Kalyvas, N.; Kandarakis, I.; Speller, R.; Nikiforidis, G. Dual energy subtraction method for breast calcification imaging. *Nucl. Instrum. Methods Phys. Res. Sect. A* **2017**, *848*, 31–38. [CrossRef]
87. Linardatos, D.; Koukou, V.; Martini, N.; Konstantinidis, A.; Bakas, A.; Fountos, G.; Valais, I.; Michail, C. On the Response of a Micro Non-Destructive Testing X-ray Detector. *Materials* **2021**, *14*, 888. [CrossRef]
88. Gong, J.K.; Arnold, J.S.; Cohn, S.H. The density of organic and volatile and non-volatile inorganic components of bone. *Anat. Rec. Adv. Integr. Anat. Evol. Biol.* **1964**, *149*, 319–324. [CrossRef] [PubMed]
89. Lemacks, M.R.; Kappadath, S.C.; Shaw, C.C.; Liu, X.; Whitman, G.J. A dual-energy subtraction technique for microcalcification imaging in digital mammography—A signal-to-noise analysis. *Med. Phys.* **2002**, *29*, 1739–1751. [CrossRef]
90. Brandan, M.-E.; Ramírez, R.V. Evaluation of dual-energy subtraction of digital mammography images under conditions found in a commercial unit. *Phys. Med. Biol.* **2006**, *51*, 2307–2320. [CrossRef]
91. Resoltech WWA Range. Clear Casting Epoxy Systems. Available online: https://www.resoltech.com/en/markets/wwa-range-detail.html (accessed on 25 February 2021).

92. Hubbell, J.H.; Seltzer, S.M. Tables of X-Ray Mass Attenuation Coefficients and Mass Energy-Absorption Coefficients 1 KeV to 20 MeV for Elements Z = 1 to 92 and 48 Additional Substances of Dosimetric Interest. 1995. Available online: http://physics.nist.gov/PhysRefData/XrayMassCoef/cover.html (accessed on 25 February 2021).
93. Available online: http://www.cirsinc.com/products/radiation-therapy/imrt-thorax-phantom/ (accessed on 25 February 2021).
94. Available online: http://www.cirsinc.com/products/ultrasound/zerdine-hydrogel/triple-modality-3d-abdominal-phantom/ (accessed on 25 February 2021).
95. Available online: http://www.cirsinc.com/products/ultrasound/zerdine-hydrogel/image-guided-abdominal-biopsy-phantom/ (accessed on 25 February 2021).
96. Available online: http://www.cirsinc.com/products/radiation-therapy/3-dimensional-torso-phantom/ (accessed on 25 February 2021).
97. Fountos, G.; Yasumura, S.; Glaros, D. The skeletal calcium/phosphorus ratio: A new in vivo method of determination. *Med. Phys.* **1997**, *24*, 1303–1310. [CrossRef]
98. Boone, J.M.; Seibert, J.A. An accurate method for computer-generating tungsten anode X-ray spectra from 30 to 140 kV. *Med. Phys.* **1997**, *24*, 1661–1670. [CrossRef]
99. Available online: https://radcal.com/ (accessed on 25 February 2021).
100. Available online: https://delmedical.com/ (accessed on 25 February 2021).
101. Koukou, V.; Martini, N.; Michail, C.; Sotiropoulou, P.; Fountzoula, C.; Kalyvas, N.; Kandarakis, I.; Nikiforidis, G.; Fountos, G. Dual Energy Method for Breast Imaging: A Simulation Study. *Comput. Math. Methods Med.* **2015**, *2015*, 1–8. [CrossRef]
102. Martini, N.; Koukou, V.; Michail, C.; Sotiropoulou, P.; Kalyvas, N.; Kandarakis, I.; Nikiforidis, G.; Fountos, G. Pencil Beam Spectral Measurements of Ce, Ho, Yb, and Ba Powders for Potential Use in Medical Applications. *J. Spectrosc.* **2015**, *2015*, 1–8. Available online: https://www.hindawi.com/journals/jspec/2015/563763/ (accessed on 25 February 2021). [CrossRef]
103. Michail, C.M.; Spyropoulou, V.A.; Fountos, G.P.; Kalyvas, N.I.; Valais, I.G.; Kandarakis, I.S.; Panayiotakis, G.S. Experimental and Theoretical Evaluation of a High Resolution CMOS Based Detector Under X-Ray Imaging Conditions. *IEEE Trans. Nucl. Sci.* **2010**, *58*, 314–322. [CrossRef]
104. Milton, R.C. An Extended Table of Critical Values for the Mann-Whitney (Wilcoxon) Two-Sample Statistic. *J. Am. Stat. Assoc.* **1964**, *59*, 925. [CrossRef]
105. Brisbane, W.; Bailey, M.R.; Sorensen, M.D. An overview of kidney stone imaging techniques. *Nat. Rev. Urol.* **2016**, *13*, 654–662. [CrossRef]
106. Pai, R.; Modh, R.; Lamoureux, R.H.; Deitte, L.; Wymer, D.C.; Mench, A.; Lipnharski, I.; Henriksen, C.; Arreola, M.; Canales, B.K. Image Quality and Patient-Specific Organ Doses in Stone Protocol CT: A Comparison of Traditional CT to Low Dose CT with Iterative Reconstruction. *BioMed Res. Int.* **2018**, *2018*, 1–6. [CrossRef] [PubMed]
107. Hokamp, N.G.; Salem, J.; Hesse, A.; Holz, J.A.; Ritter, M.; Heidenreich, A.; Maintz, D.; Haneder, S. Low-Dose Characterization of Kidney Stones Using Spectral Detector Computed Tomography: An Ex Vivo Study. *Investig. Radiol.* **2018**, *53*, 457–462. [CrossRef] [PubMed]
108. Hokamp, N.G.; Lennartz, S.; Salem, J.; Dos Santos, D.P.; Heidenreich, A.; Maintz, D.; Haneder, S. Dose independent characterization of renal stones by means of dual energy computed tomography and machine learning: An ex-vivo study. *Eur. Radiol.* **2019**, *30*, 1397–1404. [CrossRef] [PubMed]
109. Raskin, D.; Winkler, H.; Kleinmann, N.; Schor-Bardach, R.; Guranda, L.; Muzikansky, G.; Portnoy, O. Very low-dose computerized tomography for confirmation of urinary stone presence. *World J. Urol.* **2021**, *39*, 233–238. [CrossRef]
110. Morsbach, F.; Wurnig, M.C.; Müller, D.; Krauss, B.; Korporaal, J.G.; Alkadhi, H. Feasibility of Single-Source Dual-Energy Computed Tomography for Urinary Stone Characterization and Value of Iterative Reconstructions. *Investig. Radiol.* **2014**, *49*, 125–130. [CrossRef]
111. Ascenti, G.; Siragusa, C.; Racchiusa, S.; Ielo, I.; Privitera, G.; Midili, F.; Mazziotti, S. Stone-Targeted Dual-Energy CT: A New Diagnostic Approach to Urinary Calculosis. *Am. J. Roentgenol.* **2010**, *195*, 953–958. [CrossRef]
112. Eiber, M.; Holzapfel, K.; Frimberger, M.; Straub, M.; Schneider, H.; Rummeny, E.J.; Dobritz, M.; Huber, A. Targeted dual-energy single-source CT for characterisation of urinary calculi: Experimental and clinical experience. *Eur. Radiol.* **2012**, *22*, 251–258. [CrossRef] [PubMed]
113. Qu, M.; Yu, L.; Cardona, D.G.; Liu, Y.; Duan, X.; Ai, S.; Leng, S.; Shiung, M.; McCollough, C.H. Radiation Dose Reduction in Dual-Energy CT: Does It Affect the Accuracy of Urinary Stone Characterization? *Am. J. Roentgenol.* **2015**, *205*, W172–W176. [CrossRef]
114. Cheng, R.Z.; Shkolyar, E.; Chang, T.C.; Spradling, K.; Ganesan, C.; Song, S.; Pao, A.C.; Leppert, J.T.; Elliott, C.S.; To'O, K.; et al. Ultra-Low-Dose CT: An Effective Follow-Up Imaging Modality for Ureterolithiasis. *J. Endourol.* **2020**, *34*, 139–144. [CrossRef] [PubMed]
115. Kitagawa, T.; Yamamoto, H.; Nakamoto, Y.; Sasaki, K.; Toshimitsu, S.; Tatsugami, F.; Awai, K.; Hirokawa, Y.; Kihara, Y. Predictive Value of 18 F-Sodium Fluoride Positron Emission Tomography in Detecting High-Risk Coronary Artery Disease in Combination With Computed Tomography. *J. Am. Hear. Assoc.* **2018**, *7*, e010224. [CrossRef] [PubMed]
116. Kitagawa, T.; Nakamoto, Y.; Fujii, Y.; Sasaki, K.; Tatsugami, F.; Awai, K.; Hirokawa, Y.; Kihara, Y. Relationship between coronary arterial 18F-sodium fluoride uptake and epicardial adipose tissue analyzed using computed tomography. *Eur. J. Nucl. Med. Mol. Imaging* **2020**, *47*, 1746–1756. [CrossRef] [PubMed]

117. Castellano, I.A.; Nicol, E.D.; Bull, R.K.; Roobottom, C.A.; Williams, M.C.; Harden, S.P. A prospective national survey of coronary CT angiography radiation doses in the United Kingdom. *J. Cardiovasc. Comput. Tomogr.* **2017**, *11*, 268–273. [CrossRef]
118. Takagi, H.; Tanaka, R.; Nagata, K.; Ninomiya, R.; Arakita, K.; Schuijf, J.D.; Yoshioka, K. Diagnostic performance of coronary CT angiography with ultra-high-resolution CT: Comparison with invasive coronary angiography. *Eur. J. Radiol.* **2018**, *101*, 30–37. [CrossRef]
119. Jo, B.-D.; Lee, Y.-J.; Kim, D.-H.; Kim, H.-J. Scatter correction using a primary modulator for dual energy digital radiography: A Monte Carlo simulation study. *J. Korean Phys. Soc.* **2014**, *65*, 541–552. [CrossRef]
120. Ai, K.; Gao, Y.; Yu, G. A scatter correction method for dual-energy digital mammography: Monte Carlo simulation. *J. X-ray Sci. Technol.* **2014**, *22*, 653–671. [CrossRef] [PubMed]
121. Kruger, D.G.; Zink, F.; Peppler, W.W.; Ergun, D.L.; Mistretta, C.A. A regional convolution kernel algorithm for scatter correction in dual-energy images: Comparison to single-kernel algorithms. *Med. Phys.* **1994**, *21*, 175–184. [CrossRef] [PubMed]